

Wavefront restoration from lateral shearing data using spectral interpolation

SATOSHI TOMIOKA,^{1,*} NAOKI MIYAMOTO,¹ YUJI YAMAUCHI,¹ YUTAKA MATSUMOTO,¹
AND SAMIA HESHMAT²

¹ Faculty of Engineering, Hokkaido University, Sapporo 060-8628, Japan

² Faculty of Engineering, Aswan University, Aswan 81542, Egypt

* Corresponding author: tom@qe.eng.hokudai.ac.jp

Although a lateral-shear interferometer is robust against optical component vibrations, its interferogram provides information about differential wavefronts rather than the wavefronts themselves, resulting in the loss of specific frequency components. Previous studies have addressed this limitation by measuring four interferograms with different shear amounts to accurately restore the two-dimensional wavefront. This study proposes a technique that employs spectral interpolation to reduce the number of required interferograms. The proposed approach introduces an origin-shift technique for accurate spectral interpolation, which in turn is implemented by combining two methods: natural extension and least-squares determination of ambiguities in uniform biases. Numerical simulations confirmed that the proposed method accurately restored a two-dimensional wavefront from just two interferograms, thereby indicating its potential to address the limitations of the lateral-shear interferometer.

1 Introduction

A conventional interferometer utilizes two waves of light: an object wave that passes through the object under investigation and a reference wave that does not interact with the object. These waves must be nearly parallel to each other to generate a fringe pattern in an interferogram. However, when the angle of incidence on the object needs to be altered, such as in computed tomography, to measure the three-dimensional distribution of refractive index [1] using a mechanical stage, it becomes difficult to detect clear fringe patterns owing to the independent vibrations of individual optical components.

In contrast, a lateral shear interferometer (LSI) employs a sheared object wave instead of a reference wave, making it less susceptible to vibrations, considering both the sheared and original object waves experience common vibrations. However, the fringe analysis needed to obtain the wavefront in an LSI is more complex than that in a conventional interferometer.

Murty [2] proposed a simplified configuration to generate the sheared wave, wherein the object wave was obliquely incident on a parallel glass plate, resulting in two reflected waves at both the front and back surfaces. The resulting two-dimensional (2-D) interfered fringe

pattern is represented as

$$I(\mathbf{r}) = I_0(\mathbf{r}) \cos(\mathbf{k} \cdot \mathbf{r} + f(\mathbf{r})), \quad (1)$$

$$f(\mathbf{r}) = \phi(\mathbf{r} + \mathbf{s}) - \phi(\mathbf{r}), \quad (2)$$

where \mathbf{r} is the position of the point observed on the screen, \mathbf{k} is the wavenumber vector of the background fringe caused by the divergence of the incident beam and the angle of the glass plate, ϕ is the wavefront to be restored, and \mathbf{s} is the shear amount. Similar to the fringe analysis in conventional interferometry, we can obtain the phase difference $f(\mathbf{r})$ between the sheared and object waves by applying background-fringe rejection using a Fourier transform [3] and employing a phase-unwrapping method [4, 5, 6, 7, 8, 9]. To restore $\phi(\mathbf{r})$ from $f(\mathbf{r})$, we must solve Eq. (2), called the shearing problem.

Over the past five decades, several methods have been proposed to address the mathematical complexities associated with the shearing problem. These methods can be broadly classified into two categories: modal methods and zonal methods.

In modal methods, the wavefront $\phi(\mathbf{r})$ is represented by a polynomial function, such as the Zernike polynomial. The coefficients of the basis functions are estimated using least-squares fitting [10, 11, 12, 13, 14, 15]. These methods impose a limitation on the object being investigated to ensure the wavefront can be adequately represented by the polynomial function.

Conversely, zonal methods directly estimate the wavefront at the grid points. However, these methods encounter rank deficiency issues. For example, consider a one-dimensional (1-D) problem where the wavefront difference $f(x)$ is sampled at N points at intervals of Δx as

$$f_i^x = \phi_{i+n_s} - \phi_i \quad (i = \{0, 1, \dots, N-1\}), \quad (3)$$

where n_s is the number of points for the shear amount ($n_s = s/\Delta x$). In the case of $n_s = 1$, Eq. (3) can be arranged

This manuscript is the author-created manuscript, the contents of which were accepted for publication in Applied Optics by Optica Publishing Group as a Research Article on September 28, 2023. The final Publisher Version of Record has a DOI of <https://doi.org/10.1364/AO.500453> with "©2023 Optica Publishing Group. One print or electronic copy may be made for personal use only. Systematic reproduction and distribution, duplication of any material in this paper for a fee or for commercial purposes, or modifications of the content of this paper are prohibited."

as

$$\begin{aligned}\phi_n &= \phi_{n-1} + f_{n-1}^x = \phi_{n-2} + f_{n-2}^x + f_{n-1}^x = \dots \\ &= \phi_0 + \sum_{i=0}^n f_i^x.\end{aligned}\quad (4)$$

Considering the right-hand side comprises known values except for ϕ_0 , we can successively restore ϕ_n on the left-hand side if ϕ_0 is predefined. In the context of wavefront restoration, ϕ_0 represents a uniform offset of every ϕ_i which is not crucial for the restored wavefront. Considering $f^x(x)$ as the derivative of $\phi(x)$ and $\phi(x)$ as the integral of $f^x(x)$, ϕ_0 corresponds to an integral constant known as ‘piston term’ or ‘bias term.’ Similarly, in the case of $n_s \geq 2$, ϕ can be represented as

$$\phi_{n+m} = \phi_m + \sum_{j=0}^{\lfloor n/n_s \rfloor} f_{jn_s+m}^x \quad (m = \{0, 1, \dots, n_s - 1\}).\quad (5)$$

On rearranging Eq. (5), n_s unknown variables remain, which indicates that this problem is n_s -rank deficient. If we assume n_s additional equations, such as $\phi_m = 0$ for $i = \{0, \dots, n_s - 1\}$, or if the shear amount exceeds the object size by a significant margin [16, 17], we can solve all of $\phi_{i'}$ for $i' = \{0, \dots, N + n_s - 1\}$. However, this technique is not universally applicable.

In the case of a 2-D problem, $f_{i,j}^x = \phi_{i+n_s,j} - \phi_{i,j}$ for $i, j = \{0, \dots, N - 1\}$, the restored result includes n_s unknown variables for each j , which is the Nn_s -rank deficient problem. Using additional measurements with different shear directions, such as $f_{i,j}^y$ in addition to $f_{i,j}^x$, we can increase the number of equations. This effectively doubles the number of equations without increasing the number of variables, which generally indicates an overdetermined problem. However, previous studies [18, 19, 20, 21, 22, 23, 24, 25, 26, 27, 28] show that this problem cannot be solved using the least-squares method. Additionally, the set of normal equations for the least-squares problem remains rank deficient [23, 22, 25, 27, 28]. As a result, the wavefront is obtained as a minimum norm solution, which is one of the possible solutions, rather than the least-squares solution. To resolve the rank-deficient problem, a multi-shear restoration approach [29, 30, 31] that uses four interferograms with two different shears for each x and y direction has been proposed. However, the simultaneous measurement of multiple interferograms introduces complexity to the measurement system and requires specialized techniques.

Restoration methods utilizing Fourier transform [18, 32, 33, 34, 35, 36, 37, 38, 39, 40, 41, 42] are also classified as zonal methods. The Fourier transform assumes implicit periodicity, where the data within a finite domain (with a domain size of $L = N\Delta x$) is repeated outside the original domain, such as $\phi(x) = \phi(x + L)$ in the case of 1-D. This periodicity, which can be viewed as additional conditions, prevents rank deficiency issues in methods employing the Fourier transform. However, if $f(x)$ does not converge to the same value at the domain ends, the periodicity assumption becomes inappropriate, considering

$f(x)$ for $x \in [L - s, L)$ is treated as $f(x) = \phi(x + s - L) - \phi(x) \neq \phi(x + s) - \phi(x)$. This problem is known as a non-periodic or limited window problem. Elster and Weingärtner [33] demonstrated that the non-periodic problem in a 1-D shearing problem can be addressed using the ‘natural extension’ method, which involves adding data that satisfies a specific condition. Another issue that arises in Fourier transform-based restoration is that the wavefront difference $f(x)$ does not convey information about the spectral components of $\phi(x)$ of a frequency of $1/s$ and its integer multiples. This can be illustrated by the simple example of $\phi(x) = \cos(2\pi x/s)$. Here, $\phi(x)$ satisfies $\phi(x + s) = \phi(x)$; therefore, $f(x) = 0$. To tackle this problem, methods using two interferograms with different shears for each direction have been proposed [33, 34, 35, 36, 39, 41, 42], similar to zonal methods, which employ the least-squares method in the spatial domain. When the two shear amounts in each direction are coprime and combined with natural extension [34, 35], exact 2-D solutions can be restored. However, fine-tuning shear amounts in addition to multiple shear measurements would require significant experimental efforts.

Other methods have been proposed to recover the missing frequency components, including spectral interpolations using simple averaging [38] and resampling [43] techniques. These methods do not require additional difference data with varying shear amounts. However, for accurate interpolations, it is necessary for the neighboring spectrum around the frequency to be interpolated to exhibit smooth behavior. When the lost frequencies are located on a spectral tail outside the main lobe of the wavefront spectrum, the intensity of the spectrum remains smooth; however, rapid phase changes can occur in some cases. To address this issue, this study proposes a novel technique called origin shift, where the origin shift interpolation is applied to the Fourier spectrum of the 1-D difference.

Coupling the origin-shift interpolation method with natural extension can effectively restore wavefronts with minimal error. However, this method is primarily applicable to 1-D problems. To restore a 2-D wavefront, it is necessary to address the piston term problem. By utilizing a single 2-D difference data set $f_{i,j}^x$, wherein the shear is in the x direction, $\phi_{i,j}^x$ can be evaluated for each j with piston terms, $\overline{\phi_j^x}$, which cannot be determined uniquely. Similarly, the difference function $f_{i,j}^y$ measured with y -directional shear, $\phi_{i,j}^y$ has piston terms of $\overline{\phi_i^y}$. These piston terms can be determined using the least-squares method proposed by Tian *et al.* [44].

The objective of this study is to precisely restore a 2-D wavefront using only two 2-D differences acquired from different shear directions. It is important to note that each difference does not converge to the same value, which indicates a non-periodic problem. To ensure accurate reconstruction of 2-D wavefronts, we employ a combination of three methods: the natural extension method for addressing the non-periodic nature of the problem, proposed spectral interpolation with origin shift, and determining the piston terms using the least-squares method.

The remainder of this paper is organized as follows.

Section 2 provides a comprehensive review of the restoration techniques involving the Fourier transform and natural extension, along with proof of why the natural extension yields exact results. Then, we introduce the spectral interpolation approach with the origin shift. To evaluate the effectiveness of our method, we present numerical simulations for 1-D and 2-D wavefront restorations in Sec. 3. Finally, Sec. 4 discusses the key characteristics of our proposed method.

2 Wavefront Restoration Algorithm

In this section, we propose a method for restoring a 1-D wavefront from difference data by combining spectral interpolation with an origin shift technique in non-spectral space to achieve accurate spectral interpolation. The restoration is then enhanced using a natural-extension method. First, we discuss the limitations of restoration techniques based on the Fourier transform. Subsequently, we validate the correctness of the natural extension method. Finally, we present a precise spectral interpolation method employing an origin shift.

2.1 Shearing transfer function

A 1-D wavefront difference $f(x)$ acquired by measurement is defined as the difference between the wavefront $\phi(x)$ and a sheared wavefront $\phi(x+s)$ with the shear amount s as

$$f(x) = \phi(x+s) - \phi(x) \triangleq d\{\phi(x)\}, \quad (6)$$

where $d\{\}$ represents a difference operator. In the above equation, $f(x)$ and $d\{\phi(x)\}$ are also the functions of s ; however, we omit the explicit notation s for simplicity.

The Fourier transform of $f(x)$ can be expressed as the product of two functions: a specific function called the ‘shear transfer function’ that corresponds to the Fourier transform of the operator $d\{\}$ and the Fourier transform of $\phi(x)$.

Before evaluating the derivation of this relationship, we provide definitions of the Fourier transform and highlight its significant properties.

This study defines a pair of forward and inverse Fourier transforms as

$$\mathcal{F}\{a(x)\} \triangleq \int_{-\infty}^{\infty} a(x)e^{-2\pi i\kappa x} dx = A(\kappa), \quad (7)$$

$$\mathcal{F}^{-1}\{A(\kappa)\} \triangleq \int_{-\infty}^{\infty} A(\kappa)e^{+2\pi i\kappa x} d\kappa = a(x), \quad (8)$$

where i is the complex unit and κ is the wavenumber (spatial frequency) divided by the dimension of x . When the data is sampled at intervals of Δx within a finite range of $x \in \Omega = [x_0, x_0 + L)$, we obtain a discrete Fourier transform (DFT) by approximating $\int(\dots) dx \simeq$

$\sum(\dots)\Delta x$ as

$$A_m = \sum_{n=0}^{N-1} a_n e^{-2\pi i\kappa_m x_n} \Delta x \quad (m = \{m_{\min}, \dots, m_{\max}\}), \quad (9)$$

$$a_n = \sum_{m=m_{\min}}^{m_{\max}} A_m e^{+2\pi i\kappa_m x_n} \Delta \kappa \quad (n = \{0, \dots, N-1\}). \quad (10)$$

In the above equations, a_n and A_m represent $a(x_n)$ and $A(\kappa_m)$, respectively, and N represents the number of samples ($N = L/\Delta x$). To adhere to the well-known sampling theorem, m_{\min} and m_{\max} are determined using the floor and ceil functions as $m_{\min} = -\lfloor N/2 \rfloor$, $m_{\max} = \lceil N/2 \rceil - 1$, respectively. These quantities satisfy the following relations: $m_{\max} - m_{\min} = N - 1$, $\kappa_m = m\Delta\kappa$, and $\Delta\kappa = 1/L$. Going forward, the values with dimensions are measured in the sampling interval, particularly in pixels, while spatial frequencies are measured in cycles per pixel. Note that there exist periodicities

$$a_{n+lN} = a_n, \quad (11)$$

$$A_{m+lN} = A_m, \quad (12)$$

where l represents any integer, which introduces an error in the restoration of the wavefront $\phi(x)$ from the difference $f(x)$ when employing the Fourier transform. This will be discussed in detail later.

A Fourier transform of the sheared function $\phi(x+s)$ in the right-hand side of Eq. (6) can be evaluated as

$$\begin{aligned} \mathcal{F}\{\phi(x+s)\} &= \int_{-\infty}^{\infty} \phi(x+s)e^{-2\pi i\kappa x} dx \\ &= e^{2\pi i\kappa s} \int_{-\infty}^{\infty} \phi(x+s)e^{-2\pi i\kappa(x+s)} dx \\ &= e^{2\pi i\kappa s} \mathcal{F}\{\phi(x)\}. \end{aligned} \quad (13)$$

Using this relation and Eq. (6), a Fourier transform of the observed difference function, $f(x)$, can be given as

$$F(\kappa) \triangleq \mathcal{F}\{f(x)\} = D(\kappa)\mathcal{F}\{\phi(x)\}, \quad (14)$$

$$D(\kappa) = e^{2\pi i\kappa s} - 1, \quad (15)$$

where $D(\kappa)$ is the shear transfer function. In Eq. (14), $F(\kappa)$ can be computed from the observed function $f(x)$; therefore, $\phi(x)$ can be evaluated in principle as

$$\phi(x) = \mathcal{F}^{-1}\left\{\frac{F(\kappa)}{D(\kappa)}\right\}. \quad (16)$$

Equation (16) highlights a fundamental issue that is encountered by employing the Fourier transform for restoration purposes. This issue arises at $\kappa = 1/s \triangleq \kappa_s$ and its integer multiples, called ‘shear frequencies.’ The restoration of $\phi(x)$ encounters fails at shear frequencies owing to the presence of $D(\kappa)$ in the denominator of the right-hand side, resulting in a division by zero. It is important to note that both the denominator $D(\kappa)$ and numerator $F(\kappa)$ become zero at shear frequencies considering the numerator $F(\kappa)$ is lost during the measurement

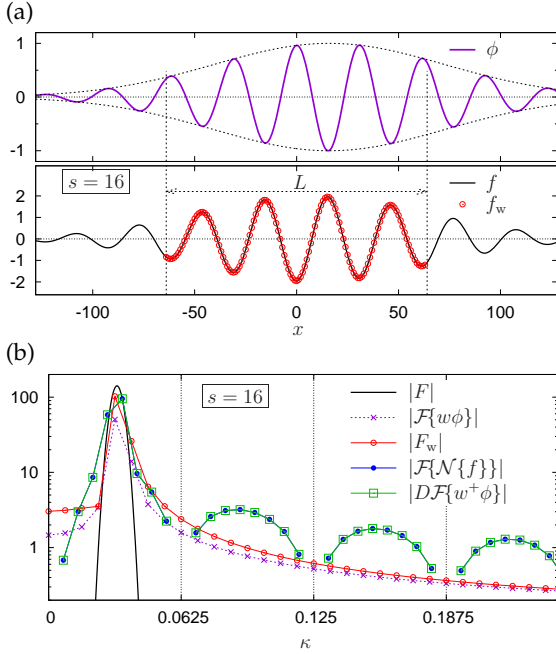


Fig. 1. Effect of the limited window on spectrum distortion: (a) Original wavefront $\phi(x)$ and corresponding wavefront difference $f(x)$ for $s=16$, with the observed data in the limited range $f_w(x)$. The range width is $[-64, 64]$ and the sampling interval is $\Delta x=1$ ($N=128$, $L=128$). Wavefront parameters are $(\lambda, x_c, w_g)=(31, 16, 80)$ for $\phi(x) = \cos(2\pi x/\lambda)e^{-(x-x_c)^2/w_g^2}$. (b) Spectral intensities related to the functions of $f(x)$, $\phi(x)$. Vertical dashed lines indicate that κ is a multiple of $1/s$.

process, as explained in Sec. 1. If we were to approach the shear frequencies by taking the limit of κ , we can determine $F(\kappa)/D(\kappa)$ for all κ and subsequently restore $\phi(x)$ using an inverse Fourier transform. The methodology illustrating this approach will be presented in detail in Sec. 2.3.

This issue can be mitigated by adjusting s to eliminate the components at the shear frequencies; i.e., $\Phi(\kappa) \simeq 0$ at $|\kappa| \geq |\kappa_s|$, which in turn we can establish $F(\kappa)/D(\kappa) = 0$ at those frequencies and achieve restoration. However, when the observed domain is limited to finite size and the periodicity of $\phi(x)$ indicated in Eq. (11) is not satisfied, significant restoration errors appear even after adjusting s . Owing to the non-periodicity, a spectral tail known as ‘leakage’ extends into the higher frequency region, thereby causing the wavefront spectrum for the finite domain to exhibit higher intensities than that of an infinite domain. Therefore, $\Phi(\kappa)$ cannot be considered zero for the limited window. One possible approach to address the non-periodic problem is elucidated in the subsequent subsection.

2.2 Natural Extension

In practical measurements, the measurement domain Ω_w is constrained to a finite range whereas the domain of the difference of $f(x)$ can be considered infinite. The observed difference is represented by multiplying it with a

window function $w(x)$, as $w(x)f(x)$, where

$$w(x) = \begin{cases} 1 & \text{for } x \in \Omega_w \\ 0 & \text{for } x \notin \Omega_w \end{cases}. \quad (17)$$

The Fourier spectrum of the finite window $F_w(\kappa)$ is determined using Eqs. (13) and (15), yielding

$$\begin{aligned} F_w(\kappa) &\triangleq \mathcal{F}\{w(x)f(x)\} \\ &= \mathcal{F}\{w(x)\phi(x+s) - w(x)\phi(x)\} \\ &= \mathcal{F}\{w(x+s)\phi(x+s) - w(x)\phi(x)\} \\ &\quad + \mathcal{F}\{(w(x) - w(x+s))\phi(x+s)\} \\ &= D(\kappa)\mathcal{F}\{w(x)\phi(x)\} + \Delta\Phi_w(\kappa), \quad (18) \\ \Delta\Phi_w(\kappa) &= \mathcal{F}\{(w(x) - w(x+s))\phi(x+s)\}. \quad (19) \end{aligned}$$

Figure 1 shows an example of $F_w(\kappa)$. Here, $\phi(x)$ shown in (a) is defined as a product of a Gaussian function and a sine function; therefore, $|\mathcal{F}\{\phi(x)\}|$ shows a Gaussian function. However, owing to the shear frequency κ_s exceeding the dominant spectral component of $\phi(x)$, no dip is observed in $|F(\kappa)|$, as denoted by the black line in (b). Within the limited domain, $|\mathcal{F}\{w(x)\phi(x)\}|$ exhibits a tail due to spectral leakage (denoted by the purple dashed line) resulting from that $w(x)\phi(x)$ does not satisfy the condition for periodicity. Despite the expectation for dips at the shear frequencies when $D(\kappa)$ is multiplied by $\mathcal{F}\{w(x)\phi(x)\}$, they are absent in $|F_w(\kappa)|$ (denoted by the red line) owing to the additional term $\Delta\Phi_w(\kappa)$ presented in Eq. (18). If $\Delta\Phi_w(\kappa) = 0$ were to be applied, $w(x)\phi(x)$ could be obtained from $F_w(\kappa)$ through the restoration process outlined in Eq. (16). In the Fourier kernel of $\Delta\Phi_w(\kappa)$, $\phi(x+s)$ is multiplied by $w(x) - w(x+s)$, which possesses a non-zero value near the ends of Ω_w . Unless the values of $\phi(x)$ at the ends coincide (satisfying the condition for periodicity), the kernel remains non-zero. This is the reason for $\Delta\Phi_w(\kappa) \neq 0$.

To cancel $\Delta\Phi_w(\kappa)$, Elster and Weingärtner [33] proposed a method called ‘natural extension.’ However, it should be noted that the representation provided below diverges from that of the original paper, because the definition of $f(x)$ has been modified.

A natural extension technique is applied when the domain size of the observed data L is an integer multiple of s . Else, L is adjusted using either a smooth extension [33] or truncation [34] before applying this technique. This study explored the characteristics of the natural extension when the data size is truncated to $\hat{L} = \lfloor L/s \rfloor s$. The appended data resulting from the natural extension are determined as follows, considering the observed wavefront difference $f(x)$ defined by Eq. (6):

$$f_{\text{ex}}(x) = - \sum_{p=1}^{\hat{L}/s} f(x+ps) \quad (x \in \Omega_{\text{ex}}). \quad (20)$$

Here, Ω_{ex} represents the domain where the additional data in the width s is appended, specifically on the negative side of $\Omega_{\hat{w}} = [x_0, x_0 + \hat{L})$ (i.e., $\Omega_{\text{ex}} = [x_0 - s, x_0)$). Notably, we chose the negative side for ease of proof;

however, the positive side of $\Omega_{\hat{w}}$ can also be selected owing to the periodic condition of the Fourier transform, as shown in Eq. (11). The data obtained after applying the natural extension can be represented as

$$\mathcal{N}\{f(x)\} = \hat{w}(x)f(x) + w_{\text{ex}}(x)f_{\text{ex}}(x), \quad (21)$$

$$\hat{w}(x) = \begin{cases} 1 & \text{for } x \in \Omega_{\hat{w}} \\ 0 & \text{for } x \notin \Omega_{\hat{w}} \end{cases}, \quad w_{\text{ex}}(x) = \begin{cases} 1 & \text{for } x \in \Omega_{\text{ex}} \\ 0 & \text{for } x \notin \Omega_{\text{ex}} \end{cases}. \quad (22)$$

The support function of observed window $\hat{w}(x)$ can be expressed as the sum of shifted functions of $w_{\text{ex}}(x)$, represented as

$$\hat{w}(x) = \sum_{p=1}^{\hat{L}/s} w_{\text{ex}}(x - ps). \quad (23)$$

Before evaluating the Fourier transform of Eq. (21), the first term on the right-hand side is rearranged using the similar procedure in the derivation of Eq. (18), yielding the modified Eq. (21) as

$$\begin{aligned} \mathcal{N}\{f(x)\} &= (\hat{w}(x+s)\phi(x+s) - \hat{w}(x)\phi(x)) \\ &\quad + (\hat{w}(x) - \hat{w}(x+s))\phi(x+s) \\ &\quad + w_{\text{ex}}(x)f_{\text{ex}}(x). \end{aligned} \quad (24)$$

The Fourier transform of the first term on the right-hand side can be evaluated as

$$\mathcal{F}\{\hat{w}(x+s)\phi(x+s) - \hat{w}(x)\phi(x)\} = (D(\kappa) - 1)\mathcal{F}\{\hat{w}(x)\phi(x)\}. \quad (25)$$

The second term on the right-hand side in Eq. (24) is expressed as two sums of shifted functions of $w_{\text{ex}}(x)$ using Eq. (23), and upon canceling common terms, it is rewritten as

$$\begin{aligned} &(\hat{w}(x) - \hat{w}(x+s))\phi(x+s) \\ &= \sum_{p=1}^{\hat{L}/s} (w_{\text{ex}}(x - ps) - w_{\text{ex}}(x - (p-1)s))\phi(x+s) \\ &= \left(\sum_{p=1}^{\hat{L}/s} w_{\text{ex}}(x - ps) - \sum_{p'=0}^{\hat{L}/s-1} w_{\text{ex}}(x - p's) \right) \phi(x+s) \\ &= w_{\text{ex}}(x - \hat{L})\phi(x+s) - w_{\text{ex}}(x)\phi(x+s). \end{aligned} \quad (26)$$

Similarly, in the third term on the right-hand side of Eq. (24), $w_{\text{ex}}(x)f_{\text{ex}}(x)$ can be substituted with

$$\begin{aligned} w_{\text{ex}}(x)f_{\text{ex}}(x) &= -w_{\text{ex}}(x) \sum_{p=1}^{\hat{L}/s} (\phi(x + (p+1)s) - \phi(x + ps)) \\ &= -w_{\text{ex}}(x)\phi(x + (\hat{L} + s)) + w_{\text{ex}}(x)\phi(x + s). \end{aligned} \quad (27)$$

The right-hand sides of Eqs. (26) and (27) contain common terms with opposite signs. The Fourier transforms of the remaining non-common terms in Eqs. (26) and (27)

are evaluated using Eq. (13) as described in

$$\begin{aligned} &\mathcal{F}\{w_{\text{ex}}(x - \hat{L})\phi(x + s)\} \\ &= e^{2\pi i \kappa s} \mathcal{F}\{w_{\text{ex}}(x - (\hat{L} + s))\phi(x)\}, \end{aligned} \quad (28)$$

$$\begin{aligned} &\mathcal{F}\{-w_{\text{ex}}(x)\phi(x + (\hat{L} + s))\} \\ &= -e^{2\pi i \kappa (\hat{L} + s)} \mathcal{F}\{w_{\text{ex}}(x - (\hat{L} + s))\phi(x)\}. \end{aligned} \quad (29)$$

When the domain size is $\hat{L} + s$, the frequency κ in the DFT is sampled so that $\kappa(\hat{L} + s)$ is an integer; therefore, the factor on the right-hand side of Eq. (29) is evaluated as

$$e^{2\pi i \kappa (\hat{L} + s)} = 1. \quad (30)$$

Consequently, the DFT of the extended data presented in Eq. (21) can be expressed as

$$\begin{aligned} \mathcal{F}\{\mathcal{N}\{f(x)\}\} &= (e^{2\pi i \kappa s} - 1)\mathcal{F}\{\hat{w}(x)\phi(x)\} \\ &\quad + (e^{2\pi i \kappa s} - 1)\mathcal{F}\{w_{\text{ex}}(x - (\hat{L} + s))\phi(x)\} \\ &= D(\kappa)\mathcal{F}\{w^+(x)\phi(x)\}, \end{aligned} \quad (31)$$

$$w^+(x) \triangleq \hat{w}(x) + w_{\text{ex}}(x - (\hat{L} + s)), \quad (32)$$

where the second term on the right-hand side of Eq. (32) represents the support for the region located outside the right-hand side of Ω_w .

Equation (31) demonstrates that the Fourier transform of the extended difference by the natural extension technique is equal to the product of the shear transfer function $D(\kappa)$ and the Fourier transform of $\phi(x)$ in the extended domain. To illustrate this equality, a numerical example is presented in Fig. 1, represented by small blue-filled circles and open green squares.

After applying the restoration procedure to Eq. (31), we obtain the relationship as

$$\mathcal{F}^{-1}\left\{\frac{\mathcal{F}\{\mathcal{N}\{f(x)\}\}}{D(\kappa)}\right\} = \hat{w}(x)\phi(x) + w_{\text{ex}}(x - (\hat{L} + s))\phi(x). \quad (33)$$

Notably, $\hat{w}(x)$ and $w_{\text{ex}}(x - (\hat{L} + s))$, for any x , do not become unity simultaneously. However, we can determine $\phi(x)$ at $x \in [x_0, x_0 + \hat{L} + s)$ by evaluating the left-hand side. This relationship reveals an interesting characteristic. The observed data domain, with a size of L , is truncated to \hat{L} , while the estimated wavefront has a wider size of $\hat{L} + s$. Because the number of data points is determined by dividing the domain size by the sampling interval, the truncated data corresponding to the input of wavefront estimation is fewer than the estimated data corresponding to the output. Despite having fewer input data points than the output, the method can accurately estimate the wavefront without errors. The unresolved issue lies in the treatment of $1/D(\kappa)$, particularly with respect to the shear harmonic frequencies.

2.3 Spectral Interpolation with Origin Shift

The components of the shear frequencies are inevitably lost during the measurement process, as demonstrated

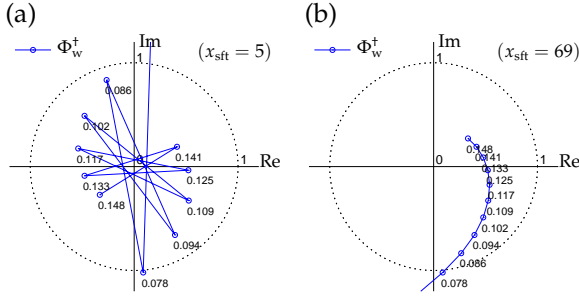


Fig. 2. The trajectory of the origin-shifted spectrum. The spectrum prior to the origin shift was evaluated by $\Phi_w(\kappa) = \mathcal{F}\{w(x)\phi(x)\}$, where $\phi(x)$ is the wavefront shown in Fig. 1(a). Origin-shifted spectrum $\Phi_w^+(\kappa)$ is obtained using Eq. (39) for (a) $x_{\text{sft}} = 5$ and (b) $x_{\text{sft}} = 69$. Numbers adjacent to points indicate corresponding frequency κ .

in Sec. 2.1. This issue can be addressed by incorporating additional difference measurements with different shear amounts [33, 34, 35, 36, 39, 41, 42]. Nevertheless, this approach increases the complexity of the measurement system. To restore these lost components using a single wavefront difference, we employ spectral interpolation.

The interpolation technique is applied to the spectrum $\Phi(\kappa)$ before applying the inverse Fourier transform, as shown in Eq. (33), where

$$\Phi(\kappa) = \frac{\mathcal{F}\{f(x)\}}{D(\kappa)}. \quad (34)$$

In this equation, when $\kappa_m \neq p\kappa_s$, where p is any integer, both the numerator and denominator on the right-hand side are already known, allowing the left-hand side to be evaluated. However, when $\kappa_m = p\kappa_s$, the spectrum needs to be interpolated from the spectra at two adjacent frequencies.

In a simple interpolation approach, the interpolated spectrum is computed as the complex plane average of the two adjacent spectral points [38], denoted as

$$\overline{\mathcal{I}}\{\Phi_m\} = \begin{cases} \overline{\Phi_m} = (\Phi_{m-1} + \Phi_{m+1})/2, & \text{for } \kappa_m = p\kappa_s, \\ \Phi_m & \text{otherwise.} \end{cases} \quad (35)$$

Nonetheless, $\overline{\Phi_m}$ introduces a significant error owing to the rapid rotation of its complex argument.

The Fourier transform, as depicted in Eq. (9), involves rearranging the equation by isolating $e^{-2\pi i\kappa_m x_0}$ outside the summation, denoted as

$$A_m = \sum_{n=0}^{N-1} a_n e^{-2\pi i\kappa_m x_n} = A_m^{(0)} e^{-2\pi i\kappa_m x_0}, \quad (36)$$

$$A_m^{(0)} = \sum_{n=0}^{N-1} a_n e^{-2\pi i\kappa_m (x_n - x_0)} = \sum_{n=0}^{N-1} a_n e^{-i\frac{2\pi m n}{N}}. \quad (37)$$

In this notation, $A_m^{(0)}$ remains independent of the origin, x_0 . Equation (36) signifies that the complex argument of A_m is the sum of the argument of $A_m^{(0)}$ and $-2\pi\kappa_m x_0$. When the origin is shifted to

$$x^+ = x - x_{\text{sft}}, \quad (38)$$

the absolute value of the spectrum remains unchanged; however, the trajectory of the spectrum in the complex plane undergoes a transformation. Figure 2 shows typical examples of these trajectories. The trajectory of the spectrum in the complex plane, as shown in Fig. 2(a), exhibits a zigzag pattern owing to rapid changes in the rotation of the complex argument of the spectrum. In contrast, the trajectory in (b) changes smoothly. The smooth variation of the trajectory offers higher accuracy for spectral interpolation at shear harmonic frequencies. The interpolation error is smaller in case (b) compared to case (a).

To achieve a smooth variation in the spectrum, an origin shift of Φ_m is applied prior to the spectral interpolation, and the origin is restored after the interpolation process. The origin-shifted spectrum is represented as

$$\Phi_m^+ = \Phi_m e^{2\pi i\kappa_m x_{\text{sft}}}. \quad (39)$$

In this equation, the origin shift x_{sft} is determined using the following algorithm to ensure a gradual change in the complex argument of Φ_m^+ .

Step 1: Evaluate the complex argument, $\theta_m = \angle\Phi_m$ for $\kappa_m \neq p\kappa_s$. The results are wrapped phases; i.e., $-1/2 \leq \theta_m < 1/2$ cycle.

Step 2: Unwrap θ_m as θ_m^u so that the absolute difference of the result between each pair of adjacent points does not exceed a half-cycle.

Step 3: Evaluate x_{sft} as a negative-averaged gradient of θ_m^u by

$$x_{\text{sft}} = -\frac{\theta_{\max\{m\}}^u - \theta_{\min\{m\}}^u}{\kappa_{\max\{m\}} - \kappa_{\min\{m\}}}. \quad (40)$$

Once the origin shift x_{sft} is acquired, the origin-shifted complex argument θ_m^+ and the origin-shifted spectrum Φ_m^+ can be evaluated as

$$\theta_m^+ = \theta_m^u + \kappa_m x_{\text{sft}}, \quad (41)$$

$$\Phi_m^+ = |\Phi_m| e^{2\pi i\theta_m^+}. \quad (42)$$

In this equation, θ_m^+ must be an unwrapped complex argument without any discontinuity larger than a half-cycle. However, if the change in the argument for $\kappa_m x_{\text{sft}}$ is significant, θ_m^+ may have jumps that exceed a half-cycle. In such situations, an additional origin shift is evaluated for the shifted Φ_m^+ using the same procedure, while Φ_m in step 1 is substituted by Φ_m^+ in Eq. (42), and the resulting x_{sft} is accumulated with the previous value.

The interpolation of the origin-shifted spectrum $\Phi_m^{\pm\hat{\mathcal{I}}}$ is evaluated by computing both the radial and angular averages of Φ_{m-1}^+ and Φ_{m+1}^+ as

$$\Phi_m^{\pm\hat{\mathcal{I}}} = \overline{|\Phi_m^+|} e^{2\pi i\overline{\theta_m^+}}, \quad (43)$$

where

$$\overline{|\Phi_m^+|} = \frac{1}{2} (|\Phi_{m-1}^+| + |\Phi_{m+1}^+|), \quad (44)$$

$$\overline{\theta_m^+} = \frac{1}{2} (\theta_{m-1}^+ + \theta_{m+1}^+). \quad (45)$$

The interpolated spectrum in the original domain is represented as

$$\widehat{\mathcal{I}}\{\Phi_m\} \triangleq \Phi_m^{\widehat{\mathcal{I}}} = \begin{cases} \Phi_m^{\widehat{\mathcal{I}}} e^{-2\pi i \kappa_m x_{\text{sft}}} & \text{for } \kappa_m = p\kappa_s, \\ \Phi_m & \text{otherwise.} \end{cases} \quad (46)$$

Spectrum interpolation allows us to determine all spectral components Φ_m , including the zero-frequency component Φ_0 . However, Φ_0 , which equals the dc component (the average of $\phi(x)$) and is referred to as the ‘piston term,’ is inherently inaccurate considering the piston term is inevitably lost during the measurement process, regardless of the shear amount s . In other words, while it can be calculated as the average of Φ_{-1} and Φ_{+1} in the spectrum interpolation, it is not significant in the experimental measurements, and hence, cannot be determined reliably. Nonetheless, because the piston term is simply uniformly added to $\phi(x)$, it is inconsequential in interferometric measurements that focus on wavefront distortion.

3 Numerical Simulations

Figure 3 shows a simulated example of wavefront restoration from a wavefront difference for $s = 14$ as an exemplary case. The observed domain size L of the wavefront difference within Ω_w is a non-integer multiple of s ($L = 128$) and requires truncation of the data to ensure \widehat{L} is a multiple of s ($\widehat{L} = 126 < L$) to apply the natural extension technique. After truncation, the natural extended data are added, resulting in $f^{\mathcal{N}}(x)$. The Fourier spectrum of the wavefront is then evaluated using $\Phi^{\mathcal{N}}(\kappa) = \mathcal{F}\{f^{\mathcal{N}}(x)\}/D(\kappa)$, which exhibits spectral leakage owing to the non-periodicity of $\phi(x)$. In this particular example, all shear harmonic frequencies are present in the spectral leakage region. A comparison is made between spectral interpolation with and without the origin shift, denoted by additional superscripts $\widehat{\mathcal{I}}$ and $\overline{\mathcal{I}}$, respectively.

The absolute spectra of $\Phi^{\mathcal{N},\widehat{\mathcal{I}}}(\kappa)$ and $\Phi^{\mathcal{N},\overline{\mathcal{I}}}(\kappa)$ are nearly identical, except for phase discrepancies at $\kappa = p\kappa_s$. The error in the restored wavefront exhibits s -periodicity, as evident from $|\Delta\Phi(\kappa)|$. This error arises solely from spectral interpolations at shear harmonic frequencies. Furthermore, the restored wavefront exhibits an ambiguity of uniform offset as the piston term corresponding to the spectrum at $\kappa = 0$ cannot be determined, as discussed in Sec. 2.3. To facilitate a comparison between the restored and true wavefronts, the piston term of the restored wavefront is determined using the following equation:

$$\phi^{\mathcal{N},\overline{\mathcal{I}}}(x) = \widetilde{\phi}^{\mathcal{N},\overline{\mathcal{I}}}(x) + \langle \phi(x) \rangle_w, \quad (47)$$

$$\widetilde{\phi}^{\mathcal{N},\overline{\mathcal{I}}}(x) = \mathcal{F}^{-1}\{\Phi^{\mathcal{N},\overline{\mathcal{I}}}(\kappa)\} - \langle \mathcal{F}^{-1}\{\Phi^{\mathcal{N},\overline{\mathcal{I}}}(\kappa)\} \rangle_w, \quad (48)$$

where $\langle \cdot \rangle_w$ represents the average of the samples in Ω_w , and the superscripts $\overline{\mathcal{I}}$ can be either $\widehat{\mathcal{I}}$ or $\overline{\mathcal{I}}$.

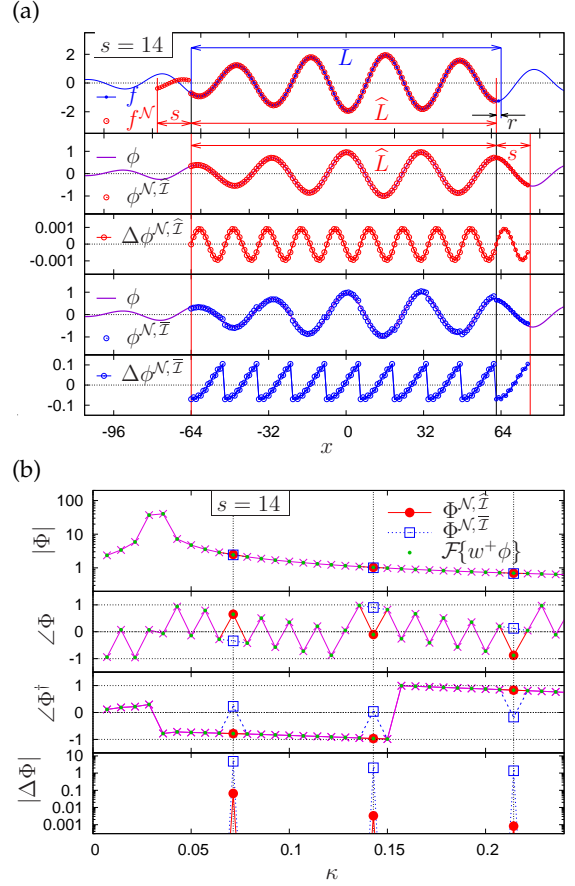


Fig. 3. Restored wavefront obtained through spectral interpolation of shearing data. (a) Analytically derived wavefront difference $f(x)$ for $s = 14$ from $\phi(x)$, where $\phi(x)$ is shown in Fig. 1. Extended data $f^{\mathcal{N}}(x) \equiv \mathcal{N}\{f(x)\}$ using natural extension through a three-step process: selection of observed domain and sampling, truncation of sampled data to ensure an integer multiple of $s/\Delta x$ points, and natural extension (indicated by small circles on the negative side of Ω_w , denoted as s). Restored wavefronts for $\Phi^{\mathcal{N},\widehat{\mathcal{I}}}(\kappa)$ and $\Phi^{\mathcal{N},\overline{\mathcal{I}}}(\kappa)$ are represented as $\phi^{\mathcal{N},\widehat{\mathcal{I}}}(x)$ and $\phi^{\mathcal{N},\overline{\mathcal{I}}}(x)$, respectively. (b) Interpolated spectrum with and without origin shift, denoted as $\Phi^{\mathcal{N},\widehat{\mathcal{I}}}(\kappa)$ and $\Phi^{\mathcal{N},\overline{\mathcal{I}}}(\kappa)$, respectively. The differences between them are only observed at $\kappa = p\kappa_s$, indicated by vertical dashed lines. The common spectrum at $\kappa \neq p\kappa_s$ is represented by cross symbols. The phase of $\Phi(\kappa)$ in the original domain and the origin-shifted domain ($x_{\text{sft}} = 73.98$) is denoted as $\angle\Phi(\kappa)$ and $\angle\Phi^+(\kappa)$, respectively. True spectrum is denoted as $\mathcal{F}\{w^+\phi(x)\}$. Quantities marked with Δ indicate differences from the true values.

The spectral error of $\Phi^{\mathcal{N},\widehat{\mathcal{I}}}(\kappa)$ is approximately two orders of magnitude smaller than that of $\Phi^{\mathcal{N},\overline{\mathcal{I}}}(\kappa)$. Consequently, when using spectral interpolation with origin shift, $\Delta\phi^{\mathcal{N},\widehat{\mathcal{I}}}(x)$, the error of the restored wavefront in the original spatial domain is significantly reduced compared to the interpolation without origin shift, $\Delta\phi^{\mathcal{N},\overline{\mathcal{I}}}(x)$. Additionally, $\phi^{\mathcal{N},\overline{\mathcal{I}}}(x)$ exhibits periodic discontinuities with a period s . In general, it is challenging to discern whether these discontinuities arise from errors or physical phenomena. Therefore, in wavefront restoration, it is crucial to achieve lower error levels while eliminating any discontinuities.

Figure 4 illustrates another example for $s = 28$. In this case, the shear frequency ($\kappa_s = 1/28 \simeq 0.0357$)

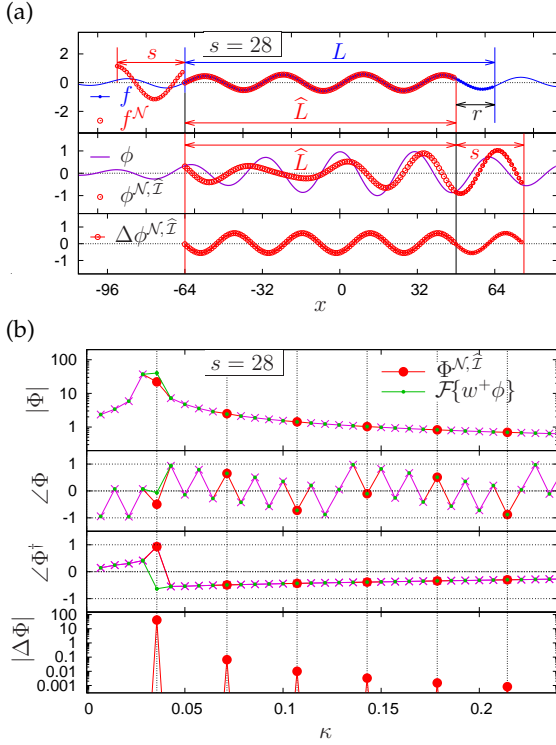


Fig. 4. Example of unsuccessful wavefront restoration. The symbols correspond to those in Fig. 3. The difference from the example in Fig. 3 is only the shear amount s ; i.e., $s = 28$ in this example. In this particular case, the shear frequency κ_s is situated within the primary lobe of the wavefront spectrum.

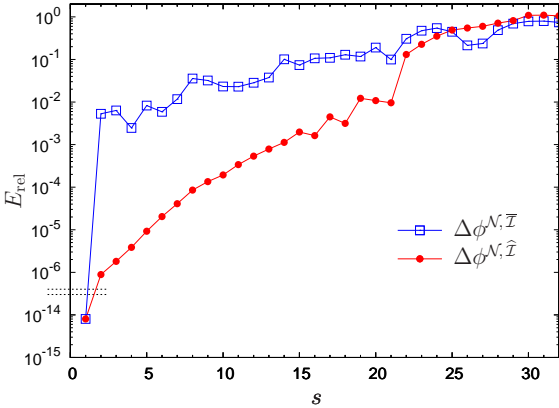


Fig. 5. Comparison of shear dependencies in restored wavefront error between spectral interpolation with and without origin shift. The vertical axis represents the normalized error, calculated as the root mean square of the true wavefront.

is located within the main lobe of the unlimited wavefront spectrum, while the shear harmonic frequencies are found in the spectral tail. In contrast to the results shown in Fig. 3 for $s = 14$, the estimation, in this case, exhibits a large error due to $\angle\Phi^\dagger(\kappa)$ at $\kappa = \kappa_s$. The peak and spectral width of the main lobe, $|\Phi(\kappa)|$, are estimated based on the parameters depicted in Fig. 1, showing a peak at $\kappa_{pk} = 1/\lambda \simeq 0.0323$ and a decrease in $1/e \simeq 0.37$ at $\kappa_{pk} \pm \delta\kappa$, where $\delta\kappa = 1/(\pi w_g) \simeq 0.0039$. The shear frequency exhibits a significant spectral inten-

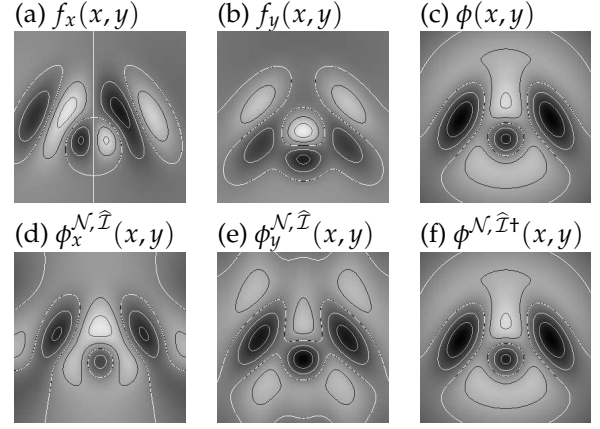


Fig. 6. Example of 2-D wavefront restoration. (a) and (b) show the 2-D difference functions using $s = (20, 0)$ and $(0, 20)$ for $\phi(x, y)$, respectively. (c) displays the true wavefront superimposed with four Gaussian functions with elliptical contour lines, (d) and (e) present the restored wavefront, where $\phi_d^{N, \hat{\mathcal{I}}}(x, y)$ (d : either x or y) is the restored wavefront obtained from $f_d(x, y)$. Each wavefront is represented by the sum of ac and dc components as $\phi_d^{N, \hat{\mathcal{I}}}(x, y) = \tilde{\phi}_d^{N, \hat{\mathcal{I}}}(x, y) + \bar{\phi}$ for comparison purposes with other wavefronts, where $\tilde{\phi}_d^{N, \hat{\mathcal{I}}}(x, y)$ represents a zero-biased wavefront obtained through natural extension combined with spectral interpolation using origin shift, and $\bar{\phi}$ corresponds to the dc component of $\phi(x, y)$; (f) illustrates the estimated wavefront after correcting piston terms using the method proposed by Tian *et al.* Both axes in all images are denoted in $[-128, 127]$. The brightness levels for (a) and (b) are indicated in $[-0.6, +0.6]$, while (c)-(f) are represented in $[-0.2, 1.0]$. The contour lines have intervals of 0.2 in all images.

sity component, $|\Phi(\kappa_s)|/|\Phi(\kappa_{pk})| \simeq 0.42$. At this frequency, two types of errors arise. First, the phase changes more rapidly around the main lobe. Second, the interpolation of intensity, as described by Eq. (44), introduces another source of error. The interpolated intensity $|\Phi_m^{\hat{\mathcal{I}}}|$ is evaluated by averaging the adjacent spectral intensities; therefore, $|\Phi_m^{\hat{\mathcal{I}}}|$ is the value between $|\Phi_{m-1}|$ and $|\Phi_{m+1}|$. This implies that spectral interpolation is suitable for cases where the spectral intensity follows a monotonically decreasing or increasing function. Conversely, when the frequency to be interpolated is located around peaks of spectral intensity distribution, significant errors may occur. In Fig. 4, the actual spectrum displayed $\Phi^{N, \hat{\mathcal{I}}}(\kappa_s) \simeq 0.3 - 22.1i \simeq |22.1|e^{-1.56i}$, while $\mathcal{F}\{w^+\phi\}_{\kappa=\kappa_s} \simeq 39.4 - 8.1i \simeq |40.3|e^{-0.20i}$; there are substantial disparities in both intensity and phase, which hinders the application of spectral interpolation. Therefore, it is necessary to choose a small shear amount s that avoids the inclusion of shear harmonic frequencies within the spectral main lobe to accurately restore wavefronts. Fortunately, selecting an appropriate s is a simple task; for instance, it can be achieved by adjusting the angle of a parallel plate relative to the optical axis in Marty's configuration.

Figure 5 illustrates the error dependencies of s by comparing the spectral interpolation methods with and without the origin shift. The error is evaluated using a relative error metric, which calculates the ratio of the root mean square error of the restored wavefront to the root mean

square of the bias-shifted true wavefront:

$$E_{\text{rel}} = \sqrt{\frac{\langle (\phi^{\mathcal{N}, \mathcal{I}}(x) - \phi(x))^2 \rangle_w}{\langle (\phi(x) - \langle \phi(x) \rangle_w)^2 \rangle_w}}. \quad (49)$$

The error increases with s , both with and without the origin shift. This phenomenon can be better understood by comparing the restored wavefronts in Figures 3 and 4. As s increases, k_s decreases and is included in the main lobe in the spectral domain. In addition, the extremely small error at $s = 1$ is owing to the Nyquist frequency κ_{max} ; i.e., $\kappa_s = 1/s > \kappa_{\text{max}}$, which makes spectral interpolation essentially unnecessary.

When reconstructing a 1-D wavefront, a certain ambiguity arises concerning the piston term. As a result, when reconstructing a 2-D wavefront from a single 2-D difference function based on the 1-D wavefront reconstruction method, no inherent information exists to establish the relationships between piston terms across various lines. To address such ambiguity, an additional 2-D difference function with a different shear direction is introduced. Figure 6 illustrates a 2-D wavefront restored using two 2-D difference functions, $f_x(x, y)$ and $f_y(x, y)$, with a shear amount of 20. These differences are computed from a true wavefront $\phi(x, y)$, consisting of the sum of four Gaussian functions featuring elliptical contour lines defined by $Ae^{-\left(\frac{\xi^2}{w_\xi^2} + \frac{\eta^2}{w_\eta^2}\right)}$ where $\xi = (x - x_c) \cos \theta + (y - y_c) \sin \theta$ and $\eta = -(x - x_c) \sin \theta + (y - y_c) \cos \theta$. The parameters of the Gaussian functions are $(A, x_c, y_c, w_\xi, w_\eta, \theta) = (1, 0, 0, 150, 150, 0), (-1, 0, -32, 30, 30, 0), (-1, \pm 64, 0, 30, 60, \pm \pi/6)$. The restored wavefront, denoted as $\tilde{\phi}_x^{\mathcal{N}, \hat{\mathcal{I}}}(x, y)$, is obtained through 1-D restoration from $f_x(x, y)$ for each y , whereas the piston term is tuned using Eq. (48), ensuring that the piston terms of $\tilde{\phi}_x^{\mathcal{N}, \hat{\mathcal{I}}}(x, y)$ are set to zero for all y . Similarly, the restored wavefront $\tilde{\phi}_y(x, y)$ obtained from $f_y(x, y)$, exhibits zero piston terms across all x .

Figures 6 (d) and (e) present the restored wavefronts with a uniform bias of $\bar{\phi} = \langle \phi(x, y) \rangle_{w_x, w_y}$ for comparison. On comparing $\tilde{\phi}_x^{\mathcal{N}, \hat{\mathcal{I}}}(x, y)$ and $\tilde{\phi}_y^{\mathcal{N}, \hat{\mathcal{I}}}(x, y)$, clear differences were noted in the restored wavefronts. Tian, Itoh, and Yatagai [44] proposed a method to determine the piston terms for x and y directions using a least-squares approach. In this method, the estimated wavefront model is given as

$$\begin{aligned} \tilde{\phi}^\dagger(x_i, y_j) &= \tilde{\phi}_x(x_i, y_j) + \bar{\phi}_x(y_j) + \epsilon_x(x_i, y_j) \\ &= \tilde{\phi}_y(x_i, y_j) + \bar{\phi}_y(x_i) + \epsilon_y(x_i, y_j), \end{aligned} \quad (50)$$

where $\tilde{\phi}^\dagger(x_i, y_j)$ represents the wavefront to be estimated, $\tilde{\phi}_x(x_i, y_j)$ and $\tilde{\phi}_y(x_i, y_j)$ are tentatively estimated wavefronts obtained through another method, and $\bar{\phi}_x(y_j)$ and $\bar{\phi}_y(x_i)$ are the piston terms to be determined, while $\epsilon_x(x_i, y_j)$ and $\epsilon_y(x_i, y_j)$ represent the residuals. The normal equations are derived to minimize $\epsilon_x^2(x_i, y_j) + \epsilon_y^2(x_i, y_j)$. If the number of samples for x and y directions is N_x and N_y , respectively, both the number

of normal equations and unknown variables ($\bar{\phi}_x(y_j)$ and $\bar{\phi}_y(x_i)$) are equal to $N_x + N_y$. However, Tian *et al.* pointed out that the normal equations are rank deficient with a rank of $N_x + N_y - 1$, which indicates that we cannot determine a 2-D piston term corresponding to a uniform offset of the 2-D wavefront. To address this issue, we replaced one of the normal equations with the following equation:

$$\langle \bar{\phi}_x(y_j) \rangle_{w_y} + \langle \bar{\phi}_y(x_i) \rangle_{w_x} = 0. \quad (51)$$

By applying this equation, the 2-D piston term of $\tilde{\phi}^\dagger(x_i, y_j)$ becomes zero. In Eqs. (50) and (51), the functions of ϕ are substituted with $\phi^{\mathcal{N}, \hat{\mathcal{I}}}$ when estimating the tentative wavefronts via the coupling of natural extension with origin-shift-based spectral interpolation. Figure (f) shows the fixed wavefront $\tilde{\phi}^{\mathcal{N}, \hat{\mathcal{I}}^\dagger}(x, y)$. A comparison between Figures (c) and (f) showed minimal error in $\phi^{\mathcal{N}, \hat{\mathcal{I}}^\dagger}(x, y)$. The relative error of $\phi^{\mathcal{N}, \hat{\mathcal{I}}^\dagger}(x, y)$, defined similarly to the 1-D restoration presented in Eq. (49), amounts to approximately 5.5×10^{-5} , while both relative errors of $\phi_x^{\mathcal{N}, \hat{\mathcal{I}}}(x, y)$ and $\phi_y^{\mathcal{N}, \hat{\mathcal{I}}}(x, y)$ are 0.57 and 0.41, respectively. In this particular example, the Fourier spectrum of $\phi(x, y)$ at the shear frequency ($|\kappa| = 1/s$) decreases to approximately 10^{-5} times the maximum spectrum, thereby indicating the application of spectral interpolations at the shear harmonic frequencies in the spectral tail region. As a result, accurate 2-D wavefront was successfully obtained by utilizing two 2-D wavefront differences of $f_x(x, y)$ and $f_y(x, y)$.

4 Conclusion

In the context of wavefront restoration from observed difference data using the Fourier transform with shear amount s , two significant problems need to be addressed. First is the loss of shear harmonic components, which correspond to spatial frequencies that are multiples of $1/s$. Second is the limited window issue, which arises when the observed data at both ends of the window fail to converge owing to the periodicity implied in the Fourier transform.

To overcome the limited window problem, this study applied the natural extension method proposed by Elster *et al.* To ensure natural extension, wherein the size of the observed data must be an integer multiple of s , we chose data truncation. We demonstrated that although the truncated data size L^\dagger is narrower than the observed domain L , we can achieve accurate restoration within a domain width of $L^\dagger + s$, which is wider than both the truncated size of L^\dagger and the observed domain size of L .

To address the loss of shear harmonic components, previous studies employed a multi-shear measurement involving different measurements with different s ; for a 2-D restoration, this typically entails four measurements, two for each of x and y . However, the use of multiple measurements for different s introduces complexity to the measurement setup. Although the application of spectral interpolation can mitigate some of these challenges, the accuracy diminishes when using a simple

spectral interpolation. To remedy this, this study proposed applying an origin shift before spectral interpolation. Shifting the origin in the original spatial domain leads to a reduction in rapid phase changes within the spectral tail, thereby providing a more accurate restoration of the wavefront. The results of 1-D numerical simulations confirmed the efficacy of coupling spectral interpolation with the origin shift technique when the recovered frequencies were located within the spectral tail. Nonetheless, if the lost frequencies overlapped with the main lobe, the accuracy decreased owing to rapid changes in both intensity and phase. This limitation can be overcome in scenarios where the wavefront of the object under investigation has a smooth profile (e.g., when the object has a smooth boundary or is composed of gas or liquid), by employing a small s , which can be easily implemented in experimental setups. Conversely, for wavefronts containing high-frequency components extending up to Nyquist frequency (e.g., when the object under investigation has a step-like profile), the proposed method cannot effectively reduce restoration errors. In this case, the complex spectrum at the lost frequency cannot be smoothly interpolated because the absolute value of the spectrum is not a smooth function even if the complex argument is. Recovering an accurate wavefront for such objects will require additional difference wavefront measurements with a different shear.

Furthermore, we extended our research to demonstrate accurate 2-D wavefront restoration using the method proposed by Tian *et al.* to determine ambiguities of piston terms in two sets of 1-D wavefronts, which are acquired with different shear directions, by utilizing a least-squares approach.

Using this combination method, an accurate 2-D wavefront can be restored from just two sheared functions with different shear directions, in contrast to previous studies that required four sheared functions. In actual measurements, especially for 2-D wavefront restoration, a fractional shear problem can arise. The approach proposed in this study is coupled with the natural extension technique that has a limitation regarding the shear amount, namely, the shear amount must be a multiple of the sampling interval, i.e., correspond to an integer shear. Although using the spectral interpolation technique allows the number of 2-D difference data to be reduced to two and eliminates the limitation mandating coprime shear amounts, the integer shear constraint, which requires more experimental efforts, persists. When the integer shear replaces the fractional shear, a non-negligible error is introduced. The reduction of this error is a future task.

In conclusion, this study demonstrated that accurate restoration of 2-D wavefronts can be achieved by employing a combined approach that involves a natural extension, spectral interpolation with origin shifting, and the least-squares method for determining piston terms. We believe the findings of this study can contribute to the field of wavefront restoration and provide valuable insights for practical implementations.

Funding This work was supported by JSPS KAKENHI Grant Number JP22K04117.

Disclosures The authors declare no potential conflicts of interest.

Data availability Data underlying the results presented in this paper are not publicly available at this time but may be obtained from the authors upon reasonable request.

References

- [1] S. Tomioka, S. Nishiyama, N. Miyamoto, D. Kando, S. Heshmat, Weighted reconstruction of three-dimensional refractive index in interferometric tomography, *Appl. Opt.* 56 (24) (2017) 6755–6764. doi:10.1364/AO.56.006755.
- [2] M. V. R. K. Murty, The use of a single plane parallel plate as a lateral shearing interferometer with a visible gas laser source, *Appl. Opt.* 3 (4) (1964) 531–534. doi:10.1364/AO.3.000531.
- [3] M. Takeda, H. Ina, S. Kobayashi, Fourier-transform method of fringe-pattern analysis for computer-based topography and interferometry, *J. Opt. Soc. Am.* 72 (1) (1982) 156–160. doi:10.1364/JOSA.72.000156.
- [4] D. C. Ghiglia, M. D. Pritt, *Two-Dimensional Phase Unwrapping: theory, algorithms, and software*, Wiley, New York, 1998.
- [5] M. Takeda, Recent progress in phase-unwrapping techniques, *Optical Inspection and Micromasurements* 2782 (1996) 334–343. doi:10.1117/12.250761.
- [6] S. Tomioka, S. Heshmat, N. Miyamoto, S. Nishiyama, Phase unwrapping for noisy phase maps using rotational compensator with virtual singular points, *Appl. Opt.* 49 (25) (2010) 4735–4745. doi:10.1364/AO.49.004735.
- [7] S. Tomioka, S. Nishiyama, Phase unwrapping for noisy phase map using localized compensator, *Appl. Opt.* 51 (21) (2012) 4984–4994. doi:10.1364/AO.51.004984.
- [8] A. Hirose, Singularity-spreading phase unwrapping: Its basic idea and the influence of time and space discreteness on the dynamics, in: *2018 Asia-Pacific Signal and Information Processing Association Annual Summit and Conference (APSIPA ASC)*, IEEE, 2018, pp. 99–103. doi:10.23919/APSIPA.2018.8659512.
- [9] S. Heshmat, S. Tomioka, S. Nishiyama, A. Hirokami, Localized compensator phase unwrapping algorithm based on flux conservative solver, *Journal of Computational Science* 62 (2022) 101752. doi:10.1016/j.jocs.2022.101752.
- [10] M. P. Rimmer, J. C. Wyant, Evaluation of large aberrations using a lateral-shear interferometer having variable shear, *Appl. Opt.* 14 (1) (1975) 142–150. doi:10.1364/AO.14.000142.
- [11] G. Harbers, P. J. Kunst, G. W. R. Leibbrandt, Analysis of lateral shearing interferograms by use of zernike polynomials, *Appl. Opt.* 35 (31) (1996) 6162–6172. doi:10.1364/AO.35.006162.
- [12] S. Okuda, T. Nomura, K. Kamiya, H. Miyashiro, K. Yoshikawa, H. Tashiro, High-precision analysis of a lateral shearing interferogram by use of the integration method and polynomials, *Appl. Opt.* 39 (28) (2000) 5179–5186. doi:10.1364/AO.39.005179.
- [13] F. Dai, F. Tang, X. Wang, O. Sasaki, M. Zhang, High spatial resolution zonal wavefront reconstruction with improved initial value determination scheme for lateral shearing interferometry, *Appl. Opt.* 52 (17) (2013) 3946–3956. doi:10.1364/AO.52.003946.
- [14] I. Mochi, K. A. Goldberg, Modal wavefront reconstruction from its gradient, *Appl. Opt.* 54 (12) (2015) 3780–3785. doi:10.1364/AO.54.003780.
- [15] T. Ling, Y. Yang, D. Liu, X. Yue, J. Jiang, J. Bai, Y. Shen, General measurement of optical system aberrations with a continuously variable lateral shear ratio by a randomly encoded hybrid grating, *Appl. Opt.* 54 (30) (2015) 8913–8920. doi:10.1364/AO.54.008913.
- [16] S. Tayal, K. Usmani, V. Singh, V. Dubey, D. Singh Mehta, Speckle-free quantitative phase and amplitude imaging using common-path lateral shearing interference microscope with pseudo-thermal light source illumination, *Optik* 180 (2019) 991–996. doi:10.1016/j.ijleo.2018.11.159.
- [17] X. Tang, Z. Cao, Z. Wang, H. Xie, L. Xu, Retrieval of phase and temperature distributions in axisymmetric flames from phase-modulated large lateral shearing interferogram, *IEEE Transactions on Instrumentation and Measurement* 70 (2021) 1–12. doi:10.1109/TIM.2021.3064804.

- [18] R. H. Hudgin, Wave-front reconstruction for compensated imaging, *J. Opt. Soc. Am.* 67 (3) (1977) 375–378. doi:10.1364/JOSA.67.000375.
- [19] D. L. Fried, Least-square fitting a wave-front distortion estimate to an array of phase-difference measurements, *J. Opt. Soc. Am.* 67 (3) (1977) 370–375. doi:10.1364/JOSA.67.000370.
- [20] R. L. Frost, C. K. Rushforth, B. S. Baxter, Fast fft-based algorithm for phase estimation in speckle imaging, *Appl. Opt.* 18 (12) (1979) 2056–2061. doi:10.1364/AO.18.002056.
- [21] B. R. Hunt, Matrix formulation of the reconstruction of phase values from phase differences, *J. Opt. Soc. Am.* 69 (3) (1979) 393–399. doi:10.1364/JOSA.69.000393.
- [22] W. Southwell, Wave-front estimation from wave-front slope measurements, *J. Opt. Soc. Am.* 70 (8) (1980) 998–1006. doi:10.1364/JOSA.70.000998.
- [23] J. Herrmann, Least-squares wave front errors of minimum norm, *J. Opt. Soc. Am.* 70 (1) (1980) 28–35. doi:10.1364/JOSA.70.000028.
- [24] R. Legarda-Sáenz, M. Rivera, R. Rodríguez-Vera, G. Trujillo-Schiaffino, Robust wave-front estimation from multiple directional derivatives, *Opt. Lett.* 25 (15) (2000) 1089–1091. doi:10.1364/OL.25.001089.
- [25] W. Zou, Z. Zhang, Generalized wave-front reconstruction algorithm applied in a shack-hartmann test, *Appl. Opt.* 39 (2) (2000) 250–268. doi:10.1364/AO.39.000250.
- [26] S.-H. Zhai, J. Ding, J. Chen, Y.-X. Fan, H.-T. Wang, Three-wave shearing interferometer based on spatial light modulator, *Opt. Express* 17 (2) (2009) 970–977. doi:10.1364/OE.17.000970.
- [27] F. Dai, F. Tang, X. Wang, O. Sasaki, Generalized zonal wave-front reconstruction for high spatial resolution in lateral shearing interferometry, *J. Opt. Soc. Am. A* 29 (9) (2012) 2038–2047. doi:10.1364/JOSAA.29.002038.
- [28] E. E. Bloemhof, Absolute surface metrology with a phase-shifting interferometer for incommensurate transverse spatial shifts, *Appl. Opt.* 53 (5) (2014) 792–797. doi:10.1364/AO.53.000792.
- [29] F. Dai, J. Li, X. Wang, Y. Bu, Exact two-dimensional zonal wave-front reconstruction with high spatial resolution in lateral shearing interferometry, *Optics Communications* 367 (2016) 264 – 273. doi:10.1016/j.optcom.2016.01.068.
- [30] D. Zhai, S. Chen, S. Xue, Z. Yin, Exact recovery of wavefront from multishearing interferograms in spatial domain, *Appl. Opt.* 55 (28) (2016) 8063–8069. doi:10.1364/AO.55.008063.
- [31] D. Zhai, S. Chen, F. Shi, High spatial resolution zonal reconstruction with modified multishear method in frequency domain, *Appl. Opt.* 56 (29) (2017) 8067–8074. doi:10.1364/AO.56.008067.
- [32] K. R. Freischlad, C. L. Koliopoulos, Modal estimation of a wave front from difference measurements using the discrete fourier transform, *J. Opt. Soc. Am. A* 3 (11) (1986) 1852–1861. doi:10.1364/JOSAA.3.001852.
- [33] C. Elster, I. Weingärtner, Solution to the shearing problem, *Appl. Opt.* 38 (23) (1999) 5024–5031. doi:10.1364/AO.38.005024.
- [34] C. Elster, I. Weingärtner, Exact wave-front reconstruction from two lateral shearing interferograms, *J. Opt. Soc. Am. A* 16 (9) (1999) 2281–2285. doi:10.1364/JOSAA.16.002281.
- [35] C. Elster, Exact two-dimensional wave-front reconstruction from lateral shearing interferograms with large shears, *Appl. Opt.* 39 (29) (2000) 5353–5359. doi:10.1364/AO.39.005353.
- [36] A. Dubra, C. Paterson, C. Dainty, Wave-front reconstruction from shear phase maps by use of the discrete fourier transform, *Appl. Opt.* 43 (5) (2004) 1108–1113. doi:10.1364/AO.43.001108.
- [37] Z. qiang Yin, S. yi Li, Exact straightness reconstruction for on-machine measuring precision workpiece, *Precision Engineering* 29 (4) (2005) 456 – 466. doi:10.1016/j.precisioneng.2004.12.012.
- [38] P. Liang, J. Ding, Z. Jin, C.-S. Guo, H. tian Wang, Two-dimensional wave-front reconstruction from lateral shearing interferograms, *Opt. Express* 14 (2) (2006) 625–634. doi:10.1364/OPEX.14.000625.
- [39] Y. feng Guo, H. Chen, J. Xu, J. Ding, Two-dimensional wavefront reconstruction from lateral multi-shear interferograms, *Opt. Express* 20 (14) (2012) 15723–15733. doi:10.1364/OE.20.015723.
- [40] Y. Guo, J. Xia, J. Ding, Recovery of wavefront from multi-shear interferograms with different tilts, *Opt. Express* 22 (10) (2014) 11407–11416. doi:10.1364/OE.22.011407.
- [41] D. Zhai, S. Chen, F. Shi, Z. Yin, Exact multi-shear reconstruction method with different tilts in spatial domain, *Optics Communications* 402 (2017) 453 – 461. doi:10.1016/j.optcom.2017.06.031.
- [42] T. Ling, J. Jiang, R. Zhang, Y. Yang, Quadriwave lateral shearing interferometric microscopy with wideband sensitivity enhancement for quantitative phase imaging in real time, *Scientific reports* 7 (1) (2017) 1–14. doi:10.1038/s41598-017-00053-7.
- [43] C. Falldorf, Y. Heimbach, C. von Kopylow, W. Jüptner, Efficient reconstruction of spatially limited phase distributions from their sheared representation, *Appl. Opt.* 46 (22) (2007) 5038–5043. doi:10.1364/AO.46.005038.
- [44] X. Tian, M. Itoh, T. Yatagai, Simple algorithm for large-grid phase reconstruction of lateral-shearing interferometry, *Appl. Opt.* 34 (31) (1995) 7213–7220. doi:10.1364/AO.34.007213.